PHYSICAL REVIEW FLUIDS **9**, 090501 (2024)

Invited Articles

Rheology of dense granular suspensions across flow regimes

Élisabeth Guazzelli*
Université Paris Cité, CNRS, Matière et Systèmes Complexes (MSC) UMR 7057, Paris, France

(Received 29 May 2024; accepted 28 August 2024; published 23 September 2024)

Dense granular suspensions, which consist of concentrated mixtures of non-Brownian particles suspended in a liquid, are ubiquitous in many natural phenomena (e.g., landslides, debris flows, and sediment transport) and industrial processes (e.g., concrete and pastes). Despite their prevalence, the rheology of these suspensions is not fully understood, and the establishment of a unified theoretical framework for different flow regimes remains a challenge. The present work reviews rheological measurements of granular suspensions in the dense regime, performed at imposed volume fractions and at imposed values of particle normal stress. It proposes a unified granular rheology over the viscous to inertial flow regime based on the superposition of inertial and viscous stress scales. This granular rheology, found for suspensions of hard spheres, can be extended to a soft granular rheology for soft particles. This soft granular rheology results in the approximate collapse of the rheological data into two branches when scaled with the distance to jamming, in a manner analogous to that found for viscous soft colloids, but now extended into the inertial regime.

DOI: 10.1103/PhysRevFluids.9.090501

I. INTRODUCTION

Dense granular suspensions are mixtures of non-Brownian particles suspended in a liquid. They are commonly found in natural phenomena and industrial processes. Examples in nature include sediment transport, such as in debris flows or landslides, or biological suspensions, such as blood, in which the red blood cells are flexible biconcave disks with a diameter of six to eight micrometers. Suspensions are found in a variety of technological and industrial processes, such as the synthesis of composite materials, pulp and paper production, and the manufacture of concrete, which is the second most widely used material in the world after water and is highly energy intensive to produce. The flow regimes in these examples range from viscous to inertial and even turbulent.

This paper presents an updated version of the Otto Laporte lecture, which was delivered at the Division of Fluid Dynamics meeting of the American Physical Society in Washington, DC, on Sunday, November 19, 2023. It describes an attempt to develop a unified theoretical framework for the rheology of dense particulate systems across different flow regimes, following and complementing the perspective review [1] written in 2018 towards this unification goal. This paper surveys rheological measurements conducted in the last six years on both rigid and soft particles, at both imposed volume fractions and imposed values of particle normal stress [2–4]. The review proposes a unified granular rheology over the viscous to inertial flow regime based on the superposition of inertial and viscous stress scales [3]. This granular rheology found for suspensions of hard spheres can be extended to a soft granular rheology for soft particles [4]. This soft granular rheology leads to an approximate collapse of the rheological data into two branches when scaled with the distance

*Contact author: elisabeth.guazzelli@u-paris.fr

to jamming, similar to that found for viscous soft colloids, but now extended into the inertial regime using stress additivity.

II. THE VISCOUS SUSPENSION RHEOLOGY

In an ambient flow, a rigid particle can have a solid-body motion that satisfies the velocity and vorticity conditions of the flow while being suspended freely, without any external force or torque. However, a rigid particle cannot respond to local deformation motion. Therefore, a freely suspended particle in an ambient flow produces a disturbance that decreases as the square of the distance from its center. This disturbance increases the dissipation of energy. The addition of particles to a fluid then results in a higher effective viscosity compared to that of the pure fluid. Einstein [5,6] employed this dissipation argument to calculate the effective viscosity of a dilute suspension of solid particles, $\eta_f(1 + 5\phi/2)$, where η_f is the viscosity of the suspending fluid and ϕ the particle volume fraction; see, for further details, Refs. [1,7].

Focusing solely on a suspension of noncolloidal, monodisperse, hard spheres at low Reynolds number, dimensional analysis reveals that the viscosity of the suspension relative to that of the suspending fluid, η_s, is solely dependent on the volume fraction, ϕ, and independent of the shear rate, $\dot{\gamma}$, as the shear stress scales viscously, $\tau = \eta_f \eta_s(\phi)\dot{\gamma}$. The suspension can then be considered a pseudo-Newtonian fluid, with viscosity increasing with increasing ϕ due to the addition of particles, as seen in Fig. 1(a), which collects typical rheological measurements and numerical simulations for noncolloidal hard frictional spheres. The linear dependence given by the Einstein viscosity, $\eta_f(1 + 5\phi/2)$, captures the experimental data only in the very dilute limit (up to $\phi \approx 0.05$). The first effect of particle pair interactions leading to correction of $O(\phi^2)$ computed by Batchelor and Green [15] can predict the semidilute limit (up to $\phi \approx 0.10$–0.15). For larger ϕ, there are no exact analytic calculations, and one must rely on numerical simulations or on phenomenological correlations such as the Maron-Pierce correlation; see, e.g., Ref. [16]. The challenge is to compute the multibody hydrodynamic interactions while simultaneously determining the microstructure. Direct mechanical contact between particles must also be taken into account. These frictional contacts due to surface roughness increase energy dissipation. As the volume fraction increases, the contribution of contact becomes more significant and dominates in the dense regime (above $\phi \approx 0.4$) [14]. This is especially evident near the jamming transition, where the viscosity diverges at ϕ_c, due to the predominance of the extended network of contacts. For the frictional particles of Fig. 1, the maximum flowable volume fraction is $\phi_c \approx 0.54$–0.62; it differs from the random close packing fraction ($\approx$0.64) seen for smooth frictionless particles and varies depending on the particle size distribution and particle frictional interactions [2].

The suspension rheology is not fully captured by the quasi-Newtonian character of the suspension viscosity we just discussed. For nondilute suspensions, normal stress differences develop, indicating that normal stresses are no longer isotropic. This non-Newtonian behavior is linked to the loss of isotropy in the suspension microstructure under shear when the concentration is increased and is also influenced by frictional particle contacts. The two normal stress differences describe the nonisotropic nature of the stress tensor; see, for further details, Refs. [1,7,17]. They are linear in the modulus of the shear rate as they are independent of the direction of the flow. Most repulsive collisions between spheres occur in the plane of shear, equally in the flow and flow-gradient directions. As a result, the second normal stress difference is negative and increases with ϕ. The first normal stress difference is much smaller, and its sign depends on the flow-induced microstructure of the particles. It is slightly negative in the bulk and positive near a wall [18].

The non-Newtonian nature of suspension flows can manifest in various ways, including particle migration phenomena in concentrated suspensions; see, for further details, Refs. [1,7,17]. For instance, in pressure-difference-induced flow, such as Poiseuille flow, neutrally buoyant particles can migrate towards the center of the pipe. The above single-fluid view is no longer appropriate when the fluid and the particles experience relative motion. This phenomenon is observed not only in the irreversible migration of particles in pipe flow but also in the erosion of sedimented beds of

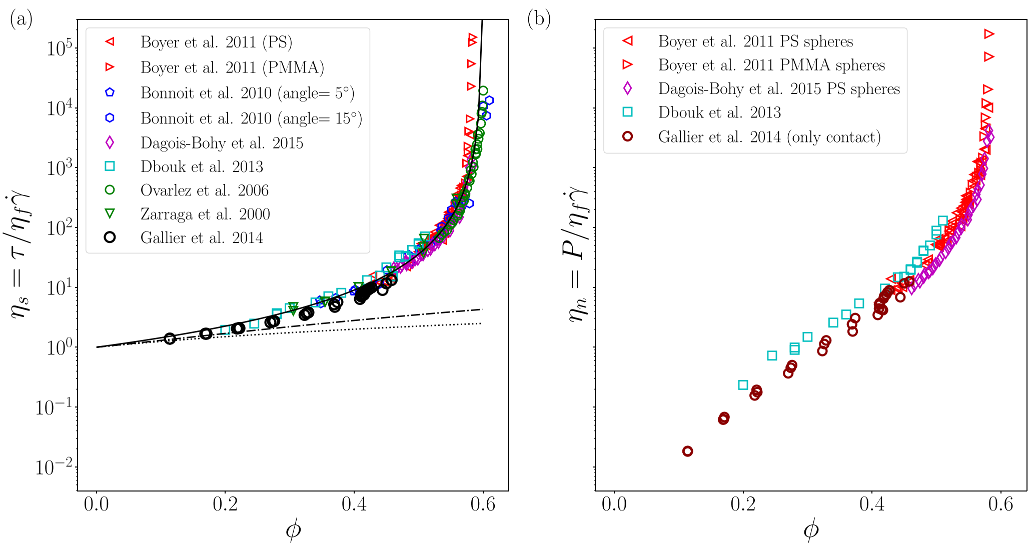

FIG. 1. Relative suspension (a) shear viscosity, η_s, and (b) normal viscosity, η_n, vs volume fraction, ϕ, for suspensions of hard frictional spheres. Experiments of Boyer *et al.* [8] using pressure-imposed rheometry with polystyrene (PS) spheres of diameter $d = 580\,\mu m$ suspended in polyethylene glycol-ran-propylene glycol monobutylether as well as poly(methyl methacrylate) (PMMA) spheres of diameter $d = 1100\,\mu m$ suspended in a Triton X-100/water/zinc chloride mixture, of Bonnoit *et al.* [9] using an inclined plane rheometer tilted at two different angles with polystyrene spheres of diameter $d = 40\,\mu m$ suspended in silicone oil, of Dagois-Bohy *et al.* [10] using pressure-imposed rheometry with polystyrene (PS) spheres of diameter $d = 580\,\mu m$ suspended in polyethylene glycol-ran-propylene glycol monobutylether, of Dbouk *et al.* [11] using a parallel-plate rotational rheometer with polystyrene spheres of diameter $d = 140\,\mu m$ suspended in a mixture of water, Ucon oil, and zinc bromide, of Ovarlez *et al.* [12] using a MRI technique and a wide-gap Couette geometry with polystyrene spheres of diameter $d = 290\,\mu m$ suspended in silicone oil, and of Zarraga *et al.* [13] using a parallel-plate rotational rheometer with glass spheres of diameter $d = 44\,\mu m$ suspended in three different fluids. Numerical simulations of Gallier *et al.* [14] with frictional spheres. Viscosity laws of Einstein [5,6] $(1 + 5\phi/2)$ (dotted line), of Batchelor and Green [15] $(1 + 5\phi/2 + 5\phi^2)$ (dashed-dotted line), and simple correlation of Maron-Pierce $(1 - \phi/\phi_c)^{-2}$ [16] (solid line). Adapted from Ref. [1].

particles under the action of shearing flows and the triggering of immersed granular avalanches. To address these situations, a two-phase approach is necessary, considering the liquid and solid phases separately [19–22]. The pressure of the particle phase is a key element in this approach.

Although the suspension mixture is incompressible, the particle phase is not. Therefore, it is important to introduce the concept of pressure of the particle phase or particle pressure, P, which is linked to the tendency of the particle phase to spread or to contract. The notion of a dispersive particle pressure under shear was early introduced by Bagnold [23] and can be considered an analog to osmotic pressure [24]. It can be seen as the nonequilibrium version of the osmotic pressure and drives the aforementioned shear-induced migration in pipe flows. Measuring particle pressure (or more generally particle normal stresses) can be challenging due to the difficulty in distinguishing between particle and fluid pressures; see, for further details, Ref. [1]. This is because the particle pressure is counterbalanced by an equal and opposite change in fluid pressure. As for the viscosity and normal stress differences of the entire suspension, particle normal stresses scale viscously and are linear in the shear rate modulus. To describe the particle normal stress, e.g., perpendicular to the shearing flow direction, a relative normal viscosity, η_n, can be introduced as $P = \eta_f \eta_n(\phi)|\dot{\gamma}|$. It is again a sole function of ϕ and presents the same divergence with ϕ as η_s when approaching jamming ($\phi \to \phi_c$), as shown in Fig. 1(b) where rheological measurements and numerical simulations are

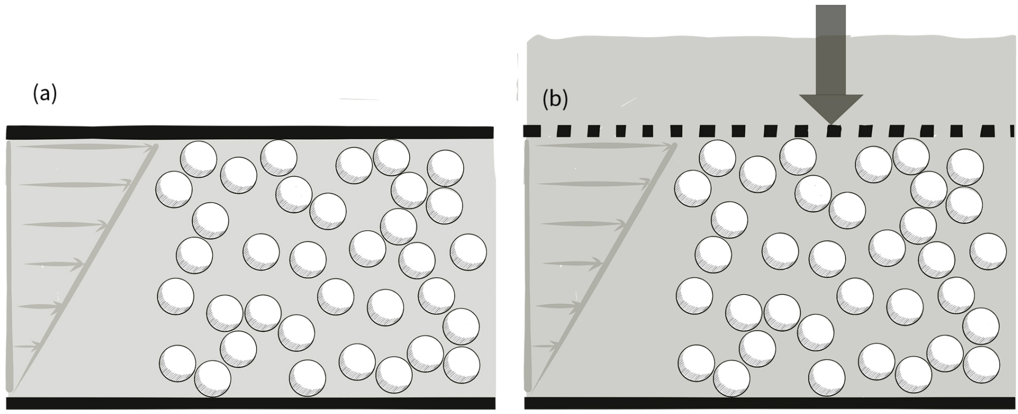

FIG. 2. Sketch of (a) volume-imposed and (b) pressure-imposed rheometry methods adapted from [1]. In volume-imposed rheometry, a suspension of neutrally buoyant particles is sheared at a constant shear rate between two roughened plates while maintaining a constant gap and volume fraction. In pressure-imposed rheometry, neutrally buoyant particles are confined between a roughened fixed lower plate and a roughened porous top plate. The top plate is moved horizontally to shear the suspension at a constant rate, while a constant vertical force is applied to it. The height of the top plate can adjust in response to dilation or compaction of the sheared suspension. The assembly of immersed particles is thus sheared at a given shear rate under a confining pressure. Adapted from Ref. [1].

presented. Importantly, in the opposite dilute limit ($\phi \to 0$), while η_s tends towards one, η_n goes to zero; η_n becomes quite small (much smaller than 0.1) when ϕ becomes smaller than 0.2.

III. GRANULAR RHEOLOGY: UNIFYING GRANULAR AND SUSPENSION FLOWS

In the previous section, we expressed the rheological laws as $\eta_s(\phi)$ and $\eta_n(\phi)$ using a single control parameter, the volume fraction ϕ. However, in the context, e.g., of sediment transport [25,26] or immersed granular avalanches [27], the volume fraction becomes a free adjustable parameter, and gravity becomes the driving force that controls the level of stress experienced by the particle phase. This rheological situation, referred to as "pressure imposed" as opposed to the previous "volume-imposed" condition, is sketched in Fig. 2. It can be shown that a granular rheology, similar to that used to describe dense dry granular flow [28], can be utilized to describe viscous suspensions [8]. In the case of a dry granular material being sheared at a shear rate $\dot{\gamma}$ under an imposed granular pressure, P, the shear stress τ is proportional to the pressure P. The effective friction coefficient $\mu = \tau/P$ and volume fraction ϕ are sole functions of the inertial number I such that $I^2 = \rho_p d^2\dot{\gamma}^2/P$ is the ratio of the inertial stress scale $\rho_p d^2\dot{\gamma}^2$ and the external confinement pressure P where d and ρ_p are, respectively, the diameter and density of the particles. The rheological law are thus given by $\mu(I)$ and $\phi(I)$. Viscous suspensions of non-Brownian spheres can be also described using this granular formalism as functions $\mu(J)$ and $\phi(J)$, where the viscous number $J = \eta_f\dot{\gamma}/P$ replaces the inertial number $I^2 = \rho_p d^2\dot{\gamma}^2/P$, i.e., the viscous stress scale $\eta_f\dot{\gamma}$ replaces the inertial stress scale $\rho_p d^2\dot{\gamma}^2$.

Pressure-imposed rheometry can be accomplished by confining the suspension in a cell and applying pressure to the grains using a top permeable plate that allows fluid to flow through but not the particles. This method was originally undertaken with a custom-built pressure imposed cell designed by [8] and then successively improved by [10,2,3]. As sketched in Fig. 2(b), the grid is moved horizontally to impose a shear rate, but its vertical position is not fixed, unlike the volume-imposed case of Fig. 2(a). A constant force is applied to the grid, and its vertical position adjusts to the flow conditions. Pressure-imposed rheometry directly measures the particle

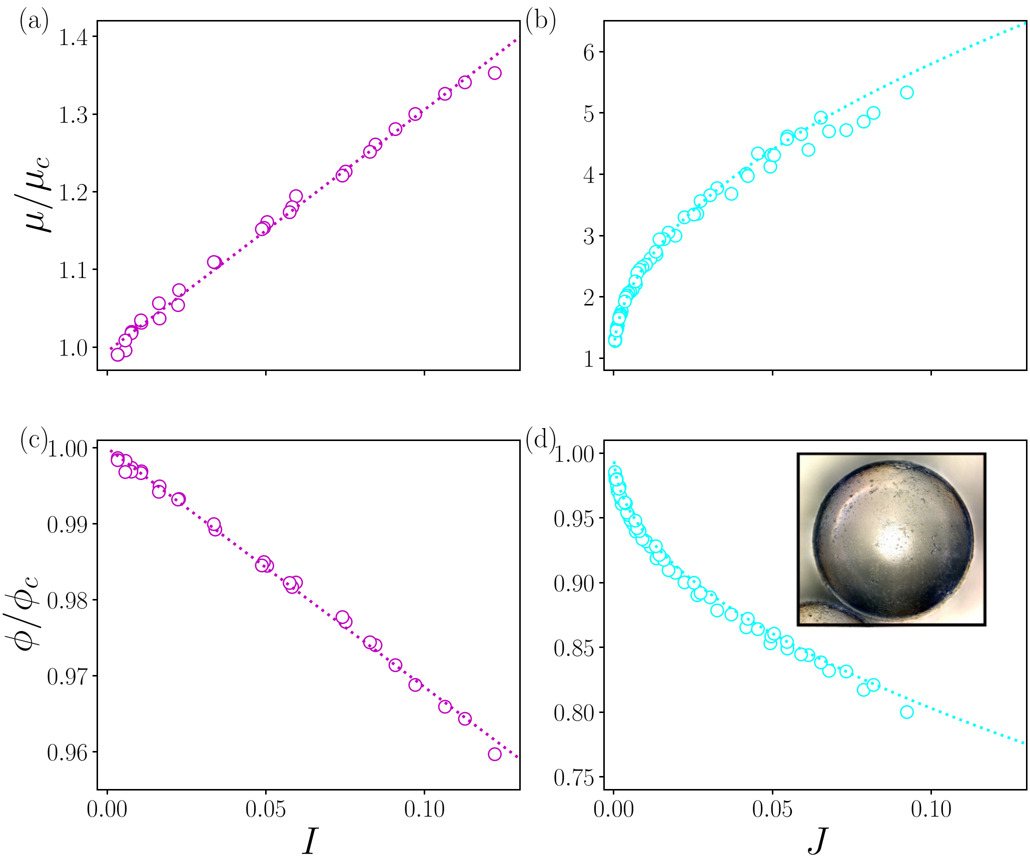

FIG. 3. (a), (b) Normalized effective friction coefficient, μ/μ_c, and (c), (d) volume fraction, ϕ/ϕ_c, vs the inertial number, $I = d\dot{\gamma}\sqrt{P/\rho_p}$, for dry polystyrene spheres (magenta color) and vs the viscous number, $J = \eta_f\dot{\gamma}/P$, for polystyrene spheres suspended in polyethylene glycol-ran-propylene glycol monobutylether (cyan color) which has a matching density with the particles ($\rho_f = 1056\,\mathrm{kg/m^3}$ at $25\,^\circ\mathrm{C}$) and a large viscosity ($\eta_f = 2.01$ Pa s at $25\,^\circ\mathrm{C}$), adapted from [2]. The dotted lines are the linear regressions in I (dry case) and $\sqrt{J}$ (immersed case). The inset in panel (d) shows a microscopic image of a typical polystyrene sphere. Adapted from Ref. [2].

pressure and consequently the suspension friction coefficient. It can also operate for very dense suspensions up to the close vicinity of jamming in a range of concentrations where the more conventional "volume-imposed" rheology usually fails. However, measurements are less accurate for dilute suspensions when the particle pressure is very small and difficult to evaluate.

Figure 3 shows pressure-imposed rheological measurements, which demonstrate that describing flow in terms of friction-coefficient and volume-fraction functions is effective for both granular flows and suspensions. The experiments are performed for the same hard frictional spheres (polystyrene spheres of diameter $d = 580\,\mu\mathrm{m}$ with average roughness $R_a = 0.29\,\mu\mathrm{m}$ and sliding and rolling interparticle friction, $\mu_{sf} = 0.24$ and $\mu_{rf} = 0.004$, respectively) in dry and immersed condition; see, for further details, Ref. [2]. The data have been normalized by their critical values at jamming, i.e., by the critical friction coefficient, μ_c, and the critical (or maximum flowable) volume fraction, ϕ_c, respectively. These critical values have been obtained by fitting the data using a linear regression in I in the dry case and in $\sqrt{J}$ in the immersed case (shown by the dotted lines). They are similar for both suspensions and dry granular media, i.e., $\phi_c = 0.585$ and $\mu_c = 0.36$ in both case, suggesting that contact forces are dominant in this quasistatic limit. As mentioned earlier in Sec. II,

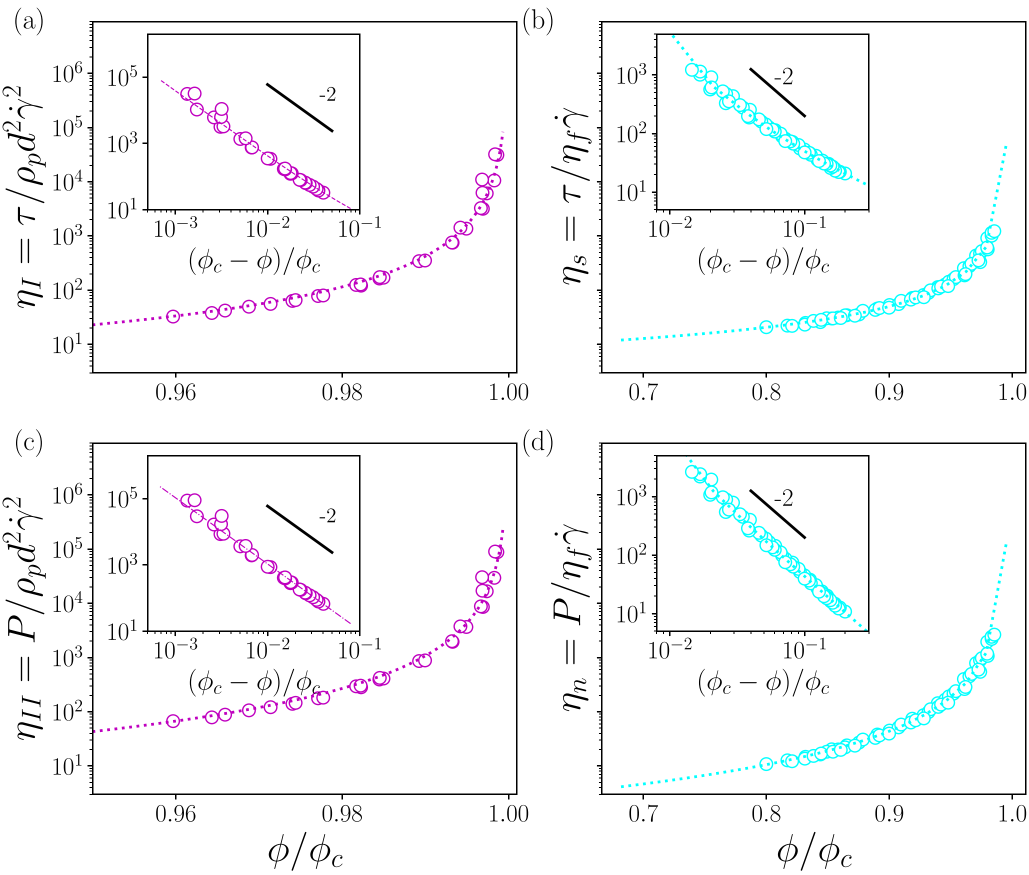

FIG. 4. (a), (b) Normalized shear stress, $\tau/\eta_f\dot\gamma$ and $\tau/\rho_p d^2\dot\gamma^2$ respectively, and (c), (d) particle normal stresses, $\tau/\eta_f\dot\gamma$ and $\tau/\rho_p d^2\dot\gamma^2$ respectively, vs ϕ/ϕ_c. The insets show the same quantities versus the rescaled volume fraction, $(\phi_c-\phi)/\phi_c$. The dotted lines correspond to the best fits using the asymptotic behaviors displayed in Fig. 3. Adapted from Ref. [2].

the value of ϕ_c depends on the nature of the frictional contacts and decreases with increasing particle roughness [2]. Interestingly, μ_c does not seem to be affected by an increase in roughness [2]. The measurements not only yield the quasistatic values but also the asymptotic behaviors of μ and ϕ in the vicinity of the jamming transition. The departures of the effective friction coefficient and of the volume fraction from their static limits, $\mu-\mu_c$ and $\phi_c-\phi$, are found to be $\propto J^\gamma$ in the immersed case and $(I^2)^\gamma$ in the dry case with same exponent $\gamma = 0.5$.

This formulation in the viscous (immersed) case is equivalent to the classical presentation in the preceding section, in which the shear and normal viscosities are a function of ϕ using $\eta_s = \tau/\eta_f\dot\gamma = \mu(J)/J$ and $\eta_n = P//\eta_f\dot\gamma = 1/J$ as shown in Figs. 4(b) and 4(d). An analogous representation for the inertial (dry) case is displayed in Figs. 4(a) and 4(c) where the shear and normal stresses are normalized by the the inertial stress scale, i.e., the Bagnold scaling $\rho_p d^2\dot\gamma^2$ [23]. This scaling defines two dimensionless functions of the volume fraction, $\eta_I = \tau/\rho_p d^2\dot\gamma^2$ and $\eta_{II} = P/\rho_p d^2\dot\gamma^2$, derived from $\eta_I = \mu/I^2$ and $\eta_{II} = 1/I^2$. All these functions are diverging as $(1-\phi/\phi_c)^{-1/\gamma}$ near jamming. Since $J = 1/\eta_n$, the relation $\eta_n \propto (1-\phi/\phi_c)^{-1/\gamma}$ seen in Fig. 4(d) confirms the relation $(\phi_c-\phi)\propto J^\gamma$ evidenced in Fig. 3(d) for the viscous case. The shear viscosity, η_s, is determined by the rheological law $\eta_s(\phi) = \mu\,\eta_n(\phi)$ and again the divergence in $(1-\phi/\phi_c)^{-1/\gamma}$ seen in Fig. 4(b) dominates close to jamming as $\mu\to\mu_c$. Similarly, the divergence of η_{II} as $(1-\phi/\phi_c)^{-1/\gamma}$ seen

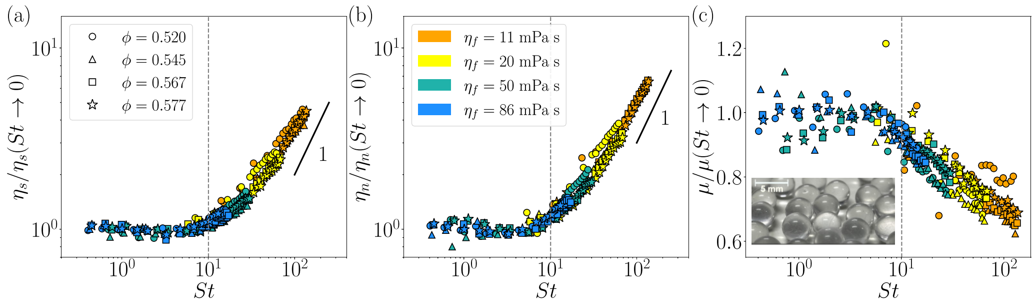

FIG. 5. (a) $\eta_s/\eta_s(\mathrm{St} \to 0)$, (b) $\eta_n/\eta_n(\mathrm{St} \to 0)$, and $\mu/\mu(\mathrm{St} \to 0)$ vs $\mathrm{St} = \rho_p d^2\dot{\gamma}/\eta_f$ for four suspensions having suspending fluids of four variable viscosities and four different volume fractions. The inset of panel (c) shows a microscopic image of the acrylic spheres. Adapted from Ref. [3].

in Fig. 4(c) is consistent with the relation $(\phi_c - \phi) \propto (I^2)^\gamma$ observed in Fig. 3(c) for the inertial case since $\eta_{II} = 1/I^2$. The other dimensionless function shown in Fig. 4(a), $\eta_I(\phi) = \mu\, \eta_{II}(\phi)$, has again a leading divergence in $(1 - \phi/\phi_c)^{-1/\gamma}$ near jamming as $\mu \to \mu_c$. The exponent $1/\gamma = 2$ is in agreement with that found in three-dimensional numerical simulations for frictional particles [29–32].

At that stage, it is important to discuss the value of the exponent that characterize the critical behavior near jamming. The critical exponent $1/\gamma = 2$, which was previously discussed, is observed in the case of frictional spheres. Increasing the surface roughness, i.e., the friction between the spheres, does not change the asymptotic behavior nor this exponent [2]. But changing the shape of the particles affects the critical behavior, and the critical exponent has been found to be $1/\gamma = 1$ for frictional fibers [33]. The critical behavior near jamming has been related to the properties of the contact network between the particles and to the analysis of the possible deformation modes of the granular packing near jamming [34]. While the role of friction remains incompletely understood, theoretical studies have been able to predict the asymptotic behavior for frictionless spheres and to identify a critical exponent of $1/\gamma = 2.83$ [34]. Experiments [35] seem to suggest a slightly larger value, $1/\gamma \approx 1/0.3 \approx 3.3$, in this later frictionless case.

IV. TRANSITION FROM NEWTONIAN TO BAGNOLDIAN RHEOLOGY: UNIFYING INERTIAL AND VISCOUS REGIMES

In the preceding section, it was shown that a comparable granular formulation can be applied to both granular and suspension flows using inertial and viscous scalings, respectively. The present section aims to go further and raises the question of whether it is possible to formulate a unified approach across these two regimes of flows which were first identified in Bagnold's seminal work [23]. It explores the transition from a viscous to an inertial regime, which is determined by the ratio of inertial to viscous stress scales, known as the Stokes number $\mathrm{St} = I^2/J = \rho_p d^2\dot{\gamma}/\eta_f$.

The rheological measurements discussed here were undertaken with the aforementioned custom rheometer, which could be run in either a pressure-imposed or a volume-imposed mode using a feedback control loop involving the particle pressure or the position of the top plate, respectively; see Fig. 2(b). The suspensions used in the experiments consisted of large hard frictional spheres (acrylic spheres of diameter $d = 4.65$ mm, average roughness $R_a = 0.29\,\mu$m, and interparticle sliding-friction coefficient $\mu_{sf} = 0.31$ in dry and water-immersed conditions but $\mu_{sf} = 0.14$ with Ucon mixtures), dispersed in a Newtonian mixture (water, Ucon oil, and some amount of sugar insuring density matching) of varying viscosity; see, for further details, Refs. [3,36].

Figure 5 shows volume-imposed rheological measurements which explore variation of St over slightly more than two decades. The ratios of shear and normal viscosities to their values at $\mathrm{St} \to 0$ show a perfect collapse when plotted against St for four different ϕ and η_f. They exhibit a (smooth)

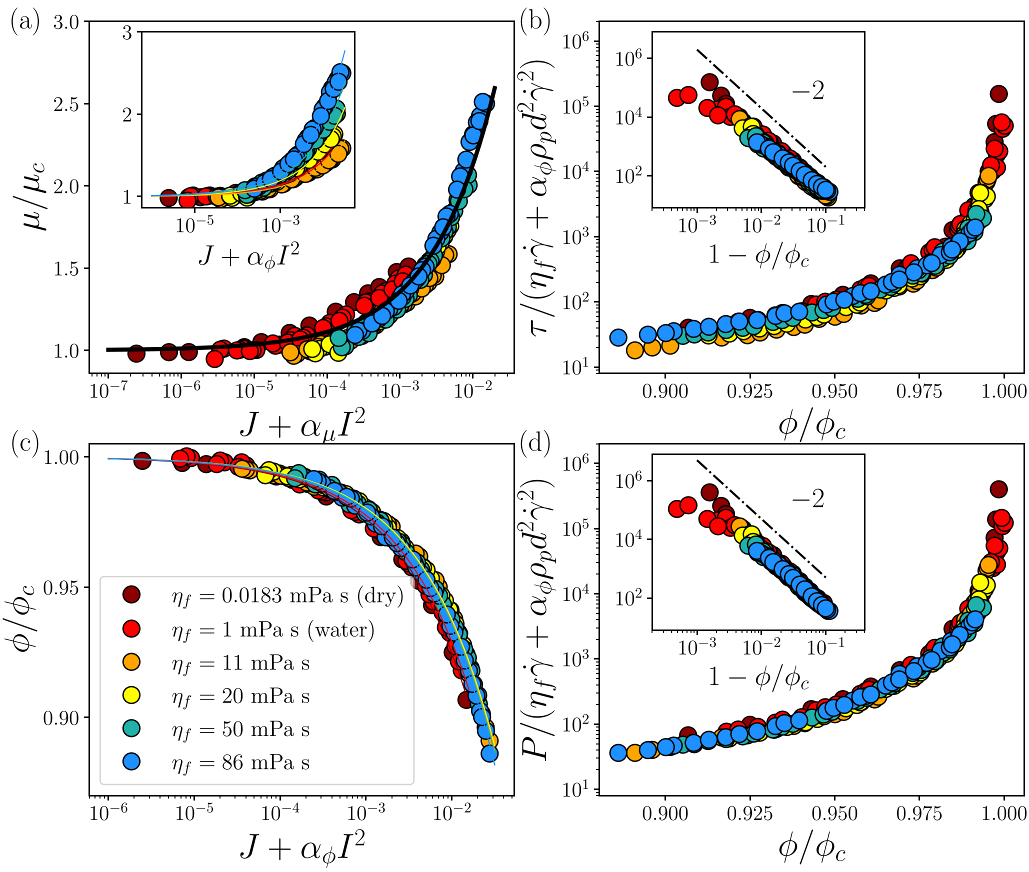

FIG. 6. (a) μ/μ_c vs $J + \alpha_\mu I^2$ (the inset shows the same quantity vs $J + \alpha_\phi I^2$) and (c) ϕ/ϕ_c vs $J + \alpha_\phi I^2$. (b) τ and (d) P normalized by $\eta_f\dot\gamma + \alpha_\phi\rho_p d^2\dot\gamma^2 = \eta_f\dot\gamma(1 + \alpha_\phi \mathrm{St})$ vs ϕ/ϕ_c (the insets show these quantities vs the rescaled volume fraction, $1 - \phi/\phi_c$. Adapted from Ref. [3].

transition from a Newtonian (slope 0) to a Bagnoldian (slope 1) rheology at a transitional Stokes number $\mathrm{St}_{v\to i} \approx 10$ independent of ϕ. This is in qualitative agreement with numerical simulations of frictional spheres [29,31,37], which, however, show a slightly smaller $\mathrm{St}_{v\to i} \approx 1 - 2$. Interestingly, the effective friction coefficient μ (which describes the anisotropy of the stresses) relative to its value at St $\to 0$ decreases with increasing St for St > 10 as η_s presents a slower transition to the Bagnoldian regime than η_n.

Figures 6(a) and 6(c) show pressure-imposed measurements for the same neutrally buoyant suspensions as in Fig. 5 and two additional negatively buoyant systems consisting of the sole dry spheres and of the spheres immersed in pure water. Following a numerical conjecture [29,31,38], the packing fraction and the effective friction have been plotted against a single dimensionless parameter based on the additivity of the stress scales J and I^2. As in Fig. 3, the data have been normalized by their critical values at jamming. While ϕ/ϕ_c is governed by the single dimensionless number $J + \alpha_\phi I^2$ with $\alpha_\phi = 1/\mathrm{St}_{v\to i} = 0.1$, μ/μ_c seems to be governed instead by $J + \alpha_\mu I^2$ with a smaller $\alpha_\mu = 0.0088$ characteristic of a larger transitional Stokes number $\mathrm{St}^\mu_{v\to i} \approx 114$. Close to jamming, the asymptotic behaviors can be expressed as

$$\frac{\phi}{\phi_c} = 1 - a_\phi (J + \alpha_\phi I^2)^{\gamma_\phi} \quad \text{with} \quad a_\phi \approx 0.66, \tag{1}$$

$$\frac{\mu}{\mu_c} = 1 + a_\mu (J + \alpha_\mu I^2)^{\gamma_\mu} \quad \text{with} \quad a_\mu \approx 11.29, \tag{2}$$

where the same exponent $\gamma = \gamma_\phi = \gamma_\mu = 0.5$ as that found in the viscous and inertial cases of Fig. 3 is recovered.

This frictional description has its dual description shown in Figs. 6(b) and 6(d) where τ and P normalized by the addition of stress scales, $\eta_f \dot{\gamma} + \alpha_\phi \rho_p d^2 \dot{\gamma}^2 = \eta_f \dot{\gamma}(1 + \alpha_\phi \mathrm{St})$, are plotted against ϕ/ϕ_c. Both functions diverge as $(1 - \phi/\phi_c)^{-2}$ close to jamming and the asymptotic behaviors deduced from Eqs. (1) and (2) can be written as

$$\frac{P}{\eta_f \dot{\gamma} + \alpha_\phi \rho_p d^2 \dot{\gamma}^2} = \left(\frac{1 - \phi/\phi_c}{a_\phi}\right)^{-\frac{1}{\gamma}}, \tag{3}$$

$$\frac{\tau}{\eta_f \dot{\gamma} + \alpha_\phi \rho_p d^2 \dot{\gamma}^2} = \mu(\phi, \mathrm{St}) \left(\frac{1 - \phi/\phi_c}{a_\phi}\right)^{-\frac{1}{\gamma}}, \tag{4}$$

$$\text{with} \quad \frac{\mu(\phi, \mathrm{St})}{\mu_c} = 1 + \frac{a_\mu}{a_\phi}\left(1 - \frac{\phi}{\phi_c}\right) \frac{(1 + \alpha_\mu \mathrm{St})^\gamma}{(1 + \alpha_\phi \mathrm{St})^\gamma}, \tag{5}$$

with the same exponent $1/\gamma = 2$ across the viscous and inertial regimes.

The difference in scaling for ϕ and μ seen in Eqs. (1) and (2) is linked to the aforementioned decrease of μ for $\mathrm{St} > 10$ evidenced in Fig. 5(c). This behavior of the stress anisotropy μ may be due to changes in the suspension microstructure and in the nature of the particle interactions when increasing inertia. This distinct finding differs from the same scaling found for ϕ and μ in the presently available numerical simulations for frictional particles [29,31,37] and requires further investigation.

V. ACROSS THE JAMMING AND VISCOUS-TO-INERTIAL TRANSITIONS: THE SOFT GRANULAR RHEOLOGY

Finally, we discuss rheological measurements of soft spherical particles, as presented in Ref. [4]. These soft particulate systems can flow beyond the jamming transition, a regime which cannot be accessed for hard grains discussed earlier in Secs. III and IV, due to the flow-induced elastic deformation of the particles [39–41]. Here we examine the rheology of soft spherical particles across jamming but also across the viscous and inertial regimes.

The particles are large polyacrylamide hydrogel spheres suspended in fluids of variable viscosity (mixtures of Ucon oil and a solution of 10% citric acid in water) and of size similar to the hard spheres discussed in Sec. IV, with a diameter ($d = 4.3$–3.2 mm) slightly decreasing with the amount of Ucon oil. The distinguishing feature is that these hydrogels are soft, with a Young's modulus ($E = 127$–232 kPa) slightly increasing with the amount of Ucon oil, and possess a low interparticle friction, with a coefficient of sliding friction $\mu_{sf} = 0.024$ when immersed in a 2% Ucon mixture; see, for further details, Ref. [4].

Due to their soft nature, the hydrogel spheres enable the system to explore states that lie both above and below the jamming transition. The effects of particle softness are equivalent to the effects of finite pressures. These finite-pressure effects can be described by a shift in the jamming packing fraction, as well as a shift in the effective friction coefficient, though to a lesser extent. These finite-pressure corrections can be accounted for by generalizing the hard-sphere granular rheology of Figs. 6(a) and 6(c), to the soft granular rheology of Figs. 7(a) and 7(c) by renormalizing the critical volume fraction and friction coefficient to pressure-dependent values [42], but still using the same values for α_ϕ and α_μ.

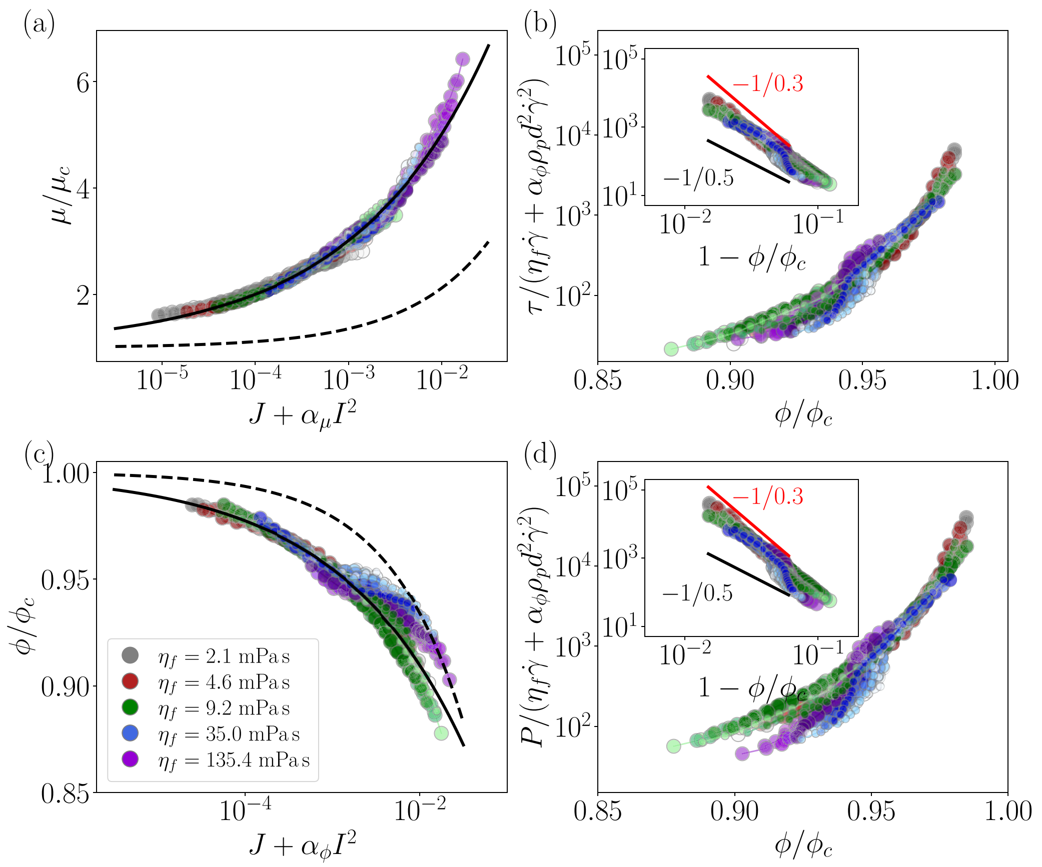

FIG. 7. (a) μ/μ_c vs $J + \alpha_\mu I^2$ and (c) ϕ/ϕ_c vs$J + \alpha_\phi I^2$. (b) τ and (d) P normalized by $\eta_f\dot\gamma + \alpha_\phi\rho_p d^2\dot\gamma^2 = \eta_f\dot\gamma(1+\alpha_\phi \mathrm{St})$ vs ϕ/ϕ_c (the insets show these quantities vs the rescaled volume fraction, $1-\phi/\phi_c$) for pressure-imposed data. The black dashed curves corresponds to the critical behavior seen in Fig. 6. An impediment to dilation is seen for the most viscous fluids for $J + \alpha_\phi I^2 \gtrsim 10^{-3}$ and is likely due to pore pressure effects. Adapted from Ref. [4].

The equations for hard spheres, Eqs. (1) and (2), are thus replaced by the new equations for soft spheres,

$$\frac{\phi}{\phi_c(\frac{P}{E})} = 1 - a_\phi (J + \alpha_\phi I^2)^{\gamma_\phi} \quad \text{with} \quad a_\phi \approx 0.36, \tag{6}$$

$$\frac{\mu}{\mu_c(\frac{P}{E})} = 1 + a_\mu (J + \alpha_\mu I^2)^{\gamma_\mu} \quad \text{with} \quad a_\mu \approx 16, \tag{7}$$

with exponent $\gamma = \gamma_\phi = \gamma_\mu = 0.3$ differing from the exponent of 0.5 found for frictional hard spheres [3] (black dashed curves) but close to that of 0.35 predicted for frictionless spheres [34]. The P dependence of $\phi_c(\frac{P}{E})$ and $\mu_c(\frac{P}{E})$ are presented in Fig. 8 and can be described by power laws [42],

$$\frac{\phi_c\left(\frac{P}{E}\right)}{\phi_c(0)} = 1 + c_\phi \left(\frac{P}{E}\right)^x, \tag{8}$$

$$\frac{\mu_c\left(\frac{P}{E}\right)}{\mu_c(0)} = 1 - c_\mu \left(\frac{P}{E}\right)^y. \tag{9}$$

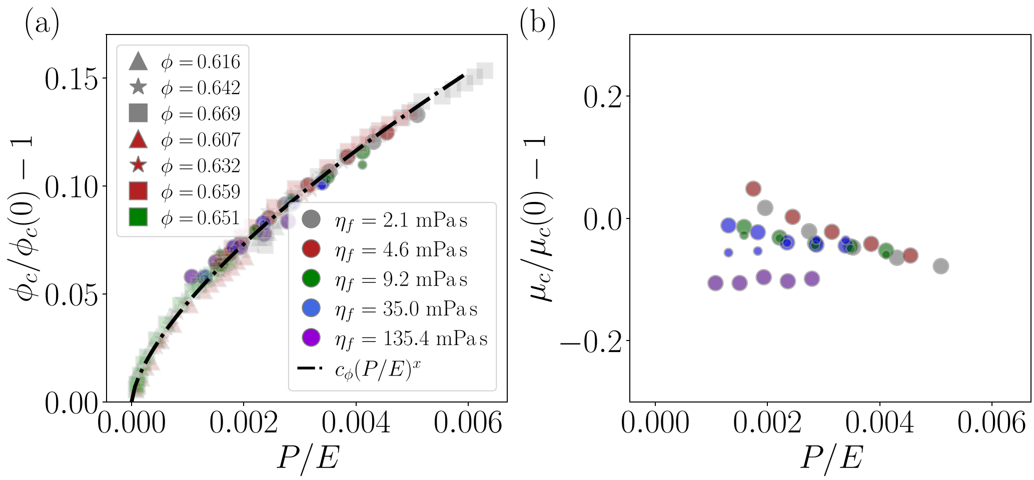

FIG. 8. (a) $\phi_c/\phi_c(0) - 1$ and $\mu_c/\mu_c(0) - 1$ vs P/E for both pressure- and volume-imposed data. Adapted from Ref. [4].

In the experiments of Ref. [4], the soft particulate system is always in the small deformation regime ($P/E \lesssim 0.007$). The increase of ϕ_c with P/E evidences Hertzian contacts as the exponent x is found to be $\approx$0.67, i.e., close to 2/3 [43]. A weak dependence is seen for μ_c which has a value $\approx \mu_c(0) \approx 0.11$ characteristic of low-friction particles. The values of $\phi_c(0)$ deduced from the fit present some variation due to experimental uncertainties (see for further details Ref. [4]) and are close to $\approx$0.64 within $\pm$5%.

As in Sec. IV, the frictional description of Figs. 7(a) and 7(c) has its dual description in Figs. 7(b) and 7(d) in which the control parameter is $\phi/\phi_c(P/E)$. But now, the asymptotic behavior of these soft and low-friction spheres differs from that of frictional particles. The normalized τ and P functions diverge as $(1-\phi/\phi_c)^{-\frac{1}{\gamma}}$ with $1/\gamma \approx 3.33$ for these low-frictional spheres instead of $(1-\phi/\phi_c)^{-\frac{1}{0.5}}$ for frictional spheres, and thus in better agreement with the theoretical predictions for frictionless spheres [29,34].

The soft granular rheology described by Eqs. (6)–(9) can be rewritten in term of normalized P and τ to account for these asymptotic diverging functions as

$$\frac{P}{\eta_f\dot{\gamma} + \alpha_\phi\rho_p d^2\dot{\gamma}^2} = \left(\frac{1-\phi/\phi_c}{a_\phi}\right)^{-\frac{1}{\gamma}} = \left\{\frac{\left[1+c_\phi\left(\frac{P}{E}\right)^x\right] - \phi/\phi_c(0)}{a_\phi\left[1+c_\phi\left(\frac{P}{E}\right)^x\right]}\right\}^{-\frac{1}{\gamma}}, \tag{10}$$

$$\frac{\tau}{\eta_f\dot{\gamma} + \alpha_\phi\rho_p d^2\dot{\gamma}^2} = \mu\left(\phi, \mathrm{St}, \frac{P}{E}\right)\frac{P}{\eta_f\dot{\gamma} + \alpha_\phi\rho_p d^2\dot{\gamma}^2}, \tag{11}$$

$$\text{with}\quad \mu\left(\phi, \mathrm{St}, \frac{P}{E}\right) = \mu_c(0)\left\{1 - c_\mu\left[\frac{\phi_c/\phi_c(0) - 1}{c_\phi}\right]^{\frac{y}{x}}\right\} \times \left[1 + a_\mu\left(\frac{P}{\eta_f\dot{\gamma} + \alpha_\phi\rho_p d^2\dot{\gamma}^2}\right)^{-\gamma}\frac{(1+\alpha_\mu \mathrm{St})^\gamma}{(1+\alpha_\phi \mathrm{St})^\gamma}\right]. \tag{12}$$

This soft granular rheology given by Eqs. (10)–(12) deduced from Eqs. (6)–(9) describes the rheology of non-Brownian soft particles on both sides of the jamming transition, accounting for the emergence of finite yield stresses (P_y and τ_y) above jamming, divergent viscosity below jamming, and shear thinning near jamming, as follows:

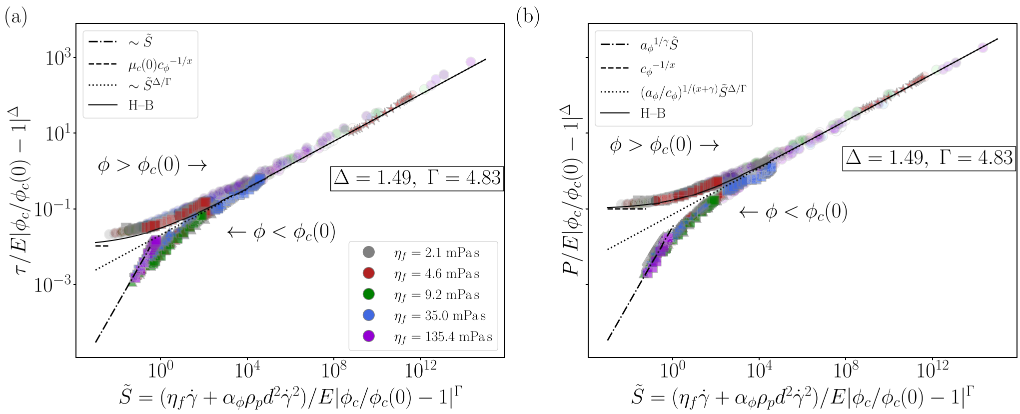

FIG. 9. Collapse of the scaled (a) τ and (b) P against the scaled addition of stress scales with $\tilde{S} = (\eta_f\dot{\gamma} + \alpha_\phi\rho_p d^2\dot{\gamma}^2)/E|1-\phi/\phi_c(0)|^\Gamma$ using the critical exponents $\Delta = 1/x$ and $\Gamma = 1/x + 1/\gamma$, for both pressure- and volume-imposed data [for $\phi > \phi_c(0) - 0.1$ to avoid sedimentation effect]. Adapted from Ref. [4].

(i) For $\phi > \phi_c(0)$ in the zero shear limit,

$$\frac{P_y}{E} = \left[\frac{\phi/\phi_c(0) - 1}{c_\phi}\right]^{\frac{1}{x}}, \tag{13}$$

$$\frac{\tau_y}{E} = \mu_c(0)\left\{1 - c_\mu\left[\frac{\phi/\phi_c(0) - 1}{c_\phi}\right]^{\frac{\gamma}{x}}\right\}\left[\frac{\phi/\phi_c(0) - 1}{c_\phi}\right]^{\frac{1}{x}}, \tag{14}$$

$$\approx \mu_c(0)\left[\frac{\phi_c/\phi_c(0) - 1}{c_\phi}\right]^{\frac{1}{x}}, \tag{15}$$

(ii) For $\phi < \phi_c(0)$ in the zero shear limit

$$\frac{P}{\eta_f\dot{\gamma} + \alpha_\phi\rho_p d^2\dot{\gamma}^2} \rightarrow \left[\frac{1 - \phi/\phi_c(0)}{a_\phi}\right]^{-1/\gamma}, \tag{16}$$

$$\frac{\tau}{\eta_f\dot{\gamma} + \alpha_\phi\rho_p d^2\dot{\gamma}^2} \rightarrow \mu_c(0)\left\{1 + \frac{a_\mu}{a_\phi}[1 - \phi/\phi_c(0)]\right\}\left[\frac{1 - \phi/\phi_c(0)}{a_\phi}\right]^{-1/\gamma}, \tag{17}$$

(iii) $\phi \rightarrow \phi_c(0)$, in the small deformation limit $c_\phi(P/E)^x \ll 1$,

$$\frac{P}{E} \rightarrow \left(\frac{a_\phi}{c_\phi}\right)^{\frac{1}{\gamma+x}}\left(\frac{\eta_f\dot{\gamma} + \alpha_\phi\rho_p d^2\dot{\gamma}^2}{E}\right)^{\frac{\gamma}{\gamma+x}}, \tag{18}$$

$$\frac{\tau}{E} \rightarrow \mu\left(\phi_c(0), \mathrm{St}, \frac{P}{E}\right)\left(\frac{a_\phi}{c_\phi}\right)^{\frac{1}{\gamma+x}}\left(\frac{\eta_f\dot{\gamma} + \alpha_\phi\rho_p d^2\dot{\gamma}^2}{E}\right)^{\frac{\gamma}{\gamma+x}}. \tag{19}$$

We can now compare the above soft granular rheology to previous scaling approaches attempting at collapsing numerical [42,44–47] and experimental [48,49] data onto two curves, one above $\phi_c(0)$ and one below. In fact, this data collapse obtained upon scaling the stresses and shear rate as power laws of the distance to jamming [44] is only approximative within this soft granular rheology framework [42]. In the small deformation limit $c_\phi(P/E)^x \ll 1$ of Ref. [4], the collapse is achieved for the particle pressure but is only approximative for the shear stress where the asymptotic behaviors are not connected by simple power laws as seen in Eqs. (14), (17), and (19).

Figure 9 presents this collapse across the viscous and inertial regimes by plotting $\tau/E|1-\phi/\phi_c(0)|^\Delta$ and $P/E|1-\phi/\phi_c(0)|^\Delta$ versus $\tilde{S}=(\eta_f\dot{\gamma}+\alpha_\phi\rho_p d^2\dot{\gamma}^2)/E|1-\phi/\phi_c(0)|^\Gamma$ for five suspensions of soft hydrogel spheres of varying viscosities. Importantly, the critical exponents $\Delta=1/x\,(\approx 1.49)$ and $\Gamma=1/x+1/y\,(\approx 4.83)$ are directly deduced from the soft granular rheology and more precisely from the asymptotic behaviors given by Eqs. (13)–(19). We can recover the different asymptotic limits described by Eqs. (13)–(19). The collapsed branch above jamming is approximately a generalized Herschel-Bulkley (H-B) law (solid curve), with yield stress given by Eqs. (13) and (14), and a shear-thinning exponent of $\Delta/\Gamma=y/(y+x)\,(=0.3)$, as shown in Eqs. (18) and (19). The collapsed branch below jamming is approximately a power law with the same exponent $\approx\Delta/\Gamma$ which merges with the upper branch in close proximity to the jamming transition (dotted line). The lower branch of the curve exhibits a linear variation given by Eqs. (16) and (17) (dashed-dotted line) at a distance from jamming, as the elastic component of the spheres becomes less dominant. It should be emphasized that the collapse was previously obtained in the viscous regime [48,49] and is now extended up to the inertial regime; see, for further details Ref. [4].

VI. CONCLUDING REMARKS

The soft granular rheology developed in Sec. V is still an empirical model, but it is remarkable in that it can describe dense suspensions over the entire size and flow range from colloidal to granular. It also includes hard granular rheology when the Young's modulus becomes very large. It is derived from an extension of the hard-sphere granular rheology described in Sec. IV and uses the natural variables of that approach, namely, the volume fraction and the effective friction coefficient. The latter may explain why the collapse is imperfect for the stresses. Interestingly, it is nearly perfect for the particle pressure, but only approximate for the shear stress. Since the shear stress is the product of the effective friction coefficient and the particle pressure, the problem seems to stem from the behavior of the effective friction coefficient.

This granular rheology provides a macroscopic framework for describing the critical behavior of suspensions near the jamming transition, as well as above and below the transition. However, the critical exponents and the coefficients involved depend on the microscopic nature of the close interactions between the particles, e.g., whether the particles are frictional or nonfrictional, or whether the contact is Hertzian or not. In this sense, the unification provided by the granular rheology is still very relative and raises the question of whether it can be fully achieved. Additionally, numerous unanswered issues remain, including why the scaling is simply the sum of the viscous and inertial stress scales, why the scaling differs for volume fraction and effective friction coefficient, and how suspension behavior (especially across the viscous-to-inertial transition) is related to the microstructure of the suspension (which is not accessible in the present rheological measurements). Furthermore, the impact of cohesive or other forces between the particles on the rheological behavior, which has not been addressed here, remains to be elucidated.

ACKNOWLEDGMENTS

This work was carried out with P. Aussillous, C.-W. Hong, O. Pouliquen, and F. Tapia (Aix-Marseille Université, CNRS, IUSTI, Marseille, France) and with M. Ichihara (Earthquake Research Institute, The University of Tokyo, Tokyo, Japan).

[1] É. Guazzelli and O. Pouliquen, Rheology of dense granular suspensions, J. Fluid Mech. **852**, P1 (2018).

[2] F. Tapia, O. Pouliquen, and É. Guazzelli, Influence of surface roughness on the rheology of immersed and dry frictional spheres, Phys. Rev. Fluids **4**, 104302 (2019).

[3] F. Tapia, M. Ichihara, O. Pouliquen, and É. Guazzelli, Viscous to inertial transition in dense granular suspension, Phys. Rev. Lett. **129**, 078001 (2022).

[4] F. Tapia, C.-W. Hong, P. Aussillous, and É. Guazzelli, Rheology of suspensions of non-Brownian soft spheres across the jamming and viscous-to-inertial transitions, Phys. Rev. Lett. **133**, 088201 (2024).

[5] A. Einstein, Eine Neue Bestimmung der Moleküldimensionen, Ann. Phys. **324**, 289 (1906).

[6] A. Einstein, Berichtigung Zu Meiner Arbeit: Eine Neue Bestimmung der Moleküldimensionen, Ann. Phys. **339**, 591 (1911).

[7] É. Guazzelli and J. F. Morris, *A Physical Introduction to Suspension Dynamics* (Cambridge University Press, Cambridge, 2012).

[8] F. Boyer, É. Guazzelli, and O. Pouliquen, Unifying suspension and granular rheology, Phys. Rev. Lett. **107**, 188301 (2011).

[9] C. Bonnoit, T. Darnige, E. Clement, and A. Lindner, Inclined plane rheometry of a dense granular suspension, J. Rheol. **54**, 65 (2010).

[10] S. Dagois-Bohy, S. Hormozi, É. Guazzelli, and O. Pouliquen, Rheology of dense suspensions of non-colloidal spheres in yield-stress fluids, J. Fluid Mech. **776**, R2 (2015).

[11] T. Dbouk, L. Lobry, and E. Lemaire, Normal stresses in concentrated non-Brownian suspensions, J. Fluid Mech. **715**, 239 (2013).

[12] G. Ovarlez, F. Bertrand, and S. Rodts, Local determination of the constitutive law of a dense suspension of noncolloidal particles through magnetic resonance imaging, J. Rheol. **50**, 259 (2006).

[13] I. E. Zarraga, D. A. Hill, and D. T. Leighton, Jr., The characterization of the total stress of concentrated suspensions of noncolloidal spheres in Newtonian fluids, J. Rheol. **44**, 185 (2000).

[14] S. Gallier, E. Lemaire, F. Peters, and L. Lobry, Rheology of sheared suspensions of rough frictional particles, J. Fluid Mech. **757**, 514 (2014).

[15] G. K. Batchelor and J. Green, The determination of the bulk stress in a suspension of spherical particles to order c^2, J. Fluid Mech. **56**, 401 (1972).

[16] J. J. Stickel and R. L. Powell, Fluid mechanics and rheology of dense suspensions, Annu. Rev. Fluid Mech. **37**, 129 (2005).

[17] M. M. Denn and J. F. Morris, Rheology of non-Brownian suspensions, Annu. Rev. Chem. Biomol. Eng. **5**, 203 (2014).

[18] S. Gallier, E. Lemaire, L. Lobry, and F. Peters, Effect of confinement in wall-bounded non-colloidal suspensions, J. Fluid Mech. **799**, 100 (2016).

[19] P. R. Nott and J. Brady, Pressure-driven flow of suspensions: Simulation and theory, J. Fluid Mech. **275**, 157 (1994).

[20] J. Morris and F. Boulay, Curvilinear flows of noncolloidal suspensions: The role of normal stresses, J. Rheol. **43**, 1213 (1999).

[21] D. Lhuillier, Migration of rigid particles in non-Brownian viscous suspensions, Phys. Fluids **21**, 023302 (2009).

[22] P. R. Nott, É. Guazzelli, and O. Pouliquen, The suspension balance model revisited, Phys. Fluids **23**, 043304 (2011).

[23] R. A. Bagnold, Experiments on a gravity-free dispersion of large solid spheres in a Newtonian fluid under shear, Proc. R. Soc. London A **225**, 49 (1954).

[24] A. Deboeuf, G. Gauthier, J. Martin, Y. Yurkovetsky, and J. F. Morris, Particle pressure in a sheared suspension: A bridge from osmosis to granular dilatancy, Phys. Rev. Lett. **102**, 108301 (2009).

[25] M. Ouriemi, P. Aussillous, and É. Guazzelli, Sediment dynamics. Part 1. Bed-load transport by laminar shearing flows, J. Fluid Mech. **636**, 295 (2009).

[26] P. Aussillous, J. Chauchat, M. Pailha, M. Médale, and É. Guazzelli, Investigation of the mobile granular layer in bedload transport by laminar shearing flows, J. Fluid Mech. **736**, 594 (2013).

[27] C. Cassar, M. Nicolas, and O. Pouliquen, Submarine granular flows down inclined planes, Phys. Fluids **17**, 103301 (2005).

[28] Y. Forterre and O. Pouliquen, Flows of dense granular media, Annu. Rev. Fluid Mech. **40**, 1 (2008).

[29] M. Trulsson, B. Andreotti, and P. Claudin, Transition from the viscous to inertial regime in dense suspensions, Phys. Rev. Lett. **109**, 118305 (2012).

[30] R. Mari, R. Seto, J. F. Morris, and M. M. Denn, Shear thickening, frictionless and frictional rheologies in non-Brownian suspensions, J. Rheol. **58**, 1693 (2014).

[31] L. Amarsid, J.-Y. Delenne, P. Mutabaruka, Y. Monerie, F. Perales, and F. Radjaï, Viscoinertial regime of immersed granular flows, Phys. Rev. E **96**, 012901 (2017).

[32] S. Gallier, F. Peters, and L. Lobry, Simulations of sheared dense noncolloidal suspensions: Evaluation of the role of long-range hydrodynamics, Phys. Rev. Fluids **3**, 042301(R) (2018).

[33] F. Tapia, S. Shaikh, J. E. Butler, O. Pouliquen, and É. Guazzelli, Rheology of concentrated suspensions of non-colloidal rigid fibres, J. Fluid Mech. **827**, R5 (2017).

[34] E. DeGiuli, G. Düring, E. Lerner, and M. Wyart, Unified theory of inertial granular flows and non-Brownian suspensions, Phys. Rev. E **91**, 062206 (2015).

[35] B. Etcheverry, Y. Forterre, and B. Metzger, Capillary-stress controlled rheometer reveals the dual rheology of shear-thickening suspensions, Phys. Rev. X **13**, 011024 (2023).

[36] F. Tapia, M. Ichihara, O. Pouliquen, and É. Guazzelli, Erratum: Viscous to inertial transition in dense granular suspension [Phys. Rev. Lett. **129**, 078001 (2022)], Phys. Rev. Lett. **131**, 109901(E) (2023).

[37] C. Ness and J. Sun, Flow regime transitions in dense non-Brownian suspensions: Rheology, microstructural characterization, and constitutive modeling, Phys. Rev. E **91**, 012201 (2015).

[38] T. T. Vo, S. Nezamabadi, P. Mutabaruka, J.-Y. Delenne, and F. Radjaï, Additive rheology of complex granular flows, Nat. Commun. **11**, 1476 (2020).

[39] J. Seth, L. Mohan, C. Locatelli-Champagne, M. Cloitre, and R. Bonnecaze, A micromechanical model to predict the flow of soft particle glasses, Nat. Mater. **10**, 838 (2011).

[40] T. Liu, F. Khabaz, R. T. Bonnecaze, and M. Cloitre, On the universality of the flow properties of soft-particle glasses, Soft Matter **14**, 7064 (2018).

[41] F. Khabaz, M. Cloitre, and R. T. Bonnecaze, Particle dynamics predicts shear rheology of soft particle glasses, J. Rheol. **64**, 459 (2020).

[42] T. Kawasaki, D. Coslovich, A. Ikeda, and L. Berthier, Diverging viscosity and soft granular rheology in non-Brownian suspensions, Phys. Rev. E **91**, 012203 (2015).

[43] C. S. O'Hern, L. E. Silbert, A. J. Liu, and S. R. Nagel, Jamming at zero temperature and zero applied stress: The epitome of disorder, Phys. Rev. E **68**, 011306 (2003).

[44] P. Olsson and S. Teitel, Critical scaling of shear viscosity at the jamming transition, Phys. Rev. Lett. **99**, 178001 (2007).

[45] T. Hatano, Scaling properties of granular rheology near the jamming transition, J. Phys. Soc. Jpn. **77**, 123002 (2008).

[46] M. Otsuki and H. Hayakawa, Critical behaviors of sheared frictionless granular materials near the jamming transition, Phys. Rev. E **80**, 011308 (2009).

[47] B. P. Tighe, E. Woldhuis, J. J. C. Remmers, W. van Saarloos, and M. van Hecke, Model for the scaling of stresses and fluctuations in flows near jamming, Phys. Rev. Lett. **105**, 088303 (2010).

[48] K. N. Nordstrom, E. Verneuil, P. E. Arratia, A. Basu, Z. Zhang, A. G. Yodh, J. P. Gollub, and D. J. Durian, Microfluidic rheology of soft colloids above and below jamming, Phys. Rev. Lett. **105**, 175701 (2010).

[49] J. Paredes, M. A. J. Michels, and D. Bonn, Rheology across the zero-temperature jamming transition, Phys. Rev. Lett. **111**, 015701 (2013).